Optimising hydroxyl airglow retrievals from long-slit astronomical spectroscopic observations

Christoph Franzen[1,2], Robert Edward Hibbins[1,2], Patrick Joseph Espy[1,2], Anlaug Amanda Djupvik[3]

[1] Norwegian University of Science and Technology (NTNU), Trondheim, 7491, Norway.
[2] Birkeland Centre for Space Science (BCSS), Norway.
[3] Nordic Optical Telescope, E-38700 Santa Cruz De La Palma, Spain

Correspondence to: Christoph Franzen (Christoph.franzen@ntnu.no)

Abstract. Astronomical spectroscopic observations from ground-based telescopes contain background emission lines from the terrestrial atmosphere's airglow. In the near infrared, this background is composed mainly of emission from Meinel bands of hydroxyl (OH), which is produced in highly excited vibrational states by reduction of ozone near 90km. This emission contains a wealth of information on the chemical and dynamical state of the Earth's atmosphere. However, observation strategies and data reduction processes are usually optimised to minimise the influence of these features on the astronomical spectrum. Here we discuss a measurement technique to optimise the extraction of the OH airglow signal itself from routine J-, H- and K-band, long-slit, astronomical spectroscopic observations. As an example, we use data recorded from a point source observation by the Nordic Optical Telescope's intermediate-resolution spectrometer, which has a spatial resolution of approximately 100 m at the airglow layer. Emission spectra from the OH vibrational manifold from $v'=9$ down to $v'=3$, with signal-to-noise ratios up to 280, have been extracted from 10.8s integrations. Rotational temperatures representative of the background atmospheric temperature near 90km, the mesosphere and lower thermosphere region, can be fitted to the OH rotational lines with an accuracy of around 0.5K. Using this measurement and analysis technique, we derive a rotational temperature distribution with v' that agrees with atmospheric model conditions and the preponderance of previous work. We discuss the derived rotational temperatures from the different vibrational bands and highlight the potential for both the archived and future observations, which are at unprecedented spatial and temporal resolutions, to contribute toward the resolution of long-standing problems in atmospheric physics.

1 Introduction

1.1 OH airglow

The atmospheric region between 85 and 90 km represents a transition zone that lies between the thermosphere, where collisions are rare, and the collision-dominated, well-mixed mesosphere. This Mesosphere and Lower Thermosphere (MLT) region is

highly variable both chemically and dynamically (Smith, 2012; Smith, 2004). It is driven from above by diurnal, seasonal and long-term changes in solar insolation, and from below by tides, planetary waves and upward propagating gravity waves. Photochemical reactions in the MLT play a key role in the vertical distribution of energy. The major loss for mesopause ozone is its reduction to molecular oxygen via:

$$H+O_3 \rightarrow OH^* +O_2 \qquad\qquad (0.1)$$
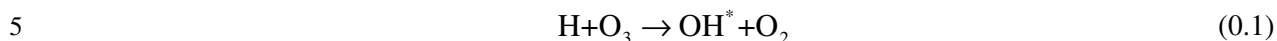
This loss is balanced by the major source of the ozone, the combination of molecular and atomic oxygen via a mediator M:

$$O+O_2+M \rightarrow O_3+M, \qquad\qquad (0.2)$$

where the atomic oxygen is formed by the dissociation of molecular oxygen by solar radiation (Espy and Stegman, 2002; Sigernes et al., 2003). Reaction (0.1) is highly exothermic (>3eV), leading to production of vibrational levels from v'=7 to v'=9 of the OH product. Deactivation of these high vibrational states primarily occurs through photo-emission in the Meinel bands (Meinel, 1950), resulting in the bright OH airglow, localized in a thick (~8 km thick) layer near 90 km, that can be observed in the visible and infrared. Collisions of each long-lived vibrational excited state (v') with the surrounding gas effectively thermalize the lower, closely spaced, rotational states into a Boltzmann distribution (Pendleton et al., 1993). Hence, moderate resolution spectroscopic measurements of the relative population of the rotational levels of individual OH vibrational bands can be used to remotely sense the temperature of the mesopause region. Furthermore, the relative intensity of the individual vibrational bands can be used to estimate the relative populations of the v' states. Comprehensive reviews on ground based observations of OH and their applications to mesopause chemistry can be found in von Zahn et al. (1987), Yee et al. (1997), and Smith et al. (2010).

However, achieving high temporal resolution has often only been possible at low spatial resolution (and vice versa). In this paper we use J-, H- and K-band, long-slit observations of an astronomical point source made by the Nordic Optical Telescope near-infrared Camera and spectrograph (NOTCam). This intermediate-resolution spectrometer was used to obtain high quality, very high spatial (<100m) resolution observations with short integration times (~10s). We demonstrate how to extract and optimise OH atmospheric spectral data from these astronomical observations, and discuss the quality and validity of the derived data over the range of vibrational bands. Finally, we consider some problems of atmospheric physics that can be addressed with these new data.

1.2 Instrumentation

Founded in 1984, and located in La Palma (17°53' W, 28°45' N), the Nordic Optical Telescope (NOT) has a primary mirror with a diameter of 2560mm (Djupvik and Andersen, 2010). Its near-infrared camera and spectrograph, NOTCam (Abbott et al., 2000), has been used for imaging since June 2001 and spectroscopy since August 2003. The detector is a 1024×1024 pixel Rockwell Science Center HgCdTe "HAWAII" array. The low resolution mode ($R = \lambda/\Delta\lambda \sim 2100$) is sufficient to resolve the individual rotational lines of an OH vibrational level. The dispersing element is an echelle grism used together with broad band filters to sort the orders. In low resolution spectroscopic mode the slit employed has a width of 128μm, corresponding to approximately 0.6 arcsec on the sky, and a slit length of 4 arcmin. At an approximate OH layer altitude of 87km (Baker and

Stair Jr., 1988), 4 arcmin corresponds to around 100m on the sky. Further details on NOTCam spectroscopy can be found in Telting (2004) and a description of the NOTCam in Djupvik (2001).

During standard astronomical observations, measurements in the *J*-, *H*- and *K*- band are typically taken. Atmospheric OH vibrational band transitions (7,4) and (8,5) are simultaneously observed in the *J*-band, the (3,1), (4,2), (5,3) and a part of the

5   (6,4) in the *H*-band, and the (8,6) and (9,7) in the *K*-band (Meinel, 1950). The (9,7) band is of particular interest as it represents the highest vibrational level populated by reaction (0.1).

2 Data reduction

To demonstrate the data reduction procedures required to optimise the OH signal from routine astronomical observations, a single *H*-band spectroscopic exposure toward a standard star, 21 Vir (spectral type B9V, H = 5.64 mag), with an exposure time

10   of 10.8s was used. This image was taken in good astronomical observing conditions at an air mass of 1.516 at 05:50:35 UT on 19 February 2013, together with dark frames and flat fields recorded with a halogen lamp on the same night. The raw image frame is reproduced in Fig. 1(a). The vertical bright band in Fig. 1(a), located slightly to the left on the detector, is the *H*-band spectrum of the star. The weaker, nearly horizontal lines that curve upward are the atmospheric OH lines from the (3,1), (4,2), (5,3) and (part of the) (6,4) vibrational bands, listed from top to bottom in the image frame.

15   For the initial data reduction steps standard IRAF (Tody, 1993) astronomical procedures were followed. This entailed removing bad pixels (zero valued or cold) that are known and stable, and dark frames were used to create a pixel mask to remove hot pixels on the detector. The intensity of the OH lines is well within the linear range of the array, so non-linearity effects could be ignored. The dark current was removed using dark images taken toward the closed dome before observations began. Wavelength dependent variations in transmission and detector response were corrected by flat fielding using short integrations

20   of a halogen lamp situated at the upper end of the optical path.

The stellar spectrum is much brighter than the OH lines and has to be removed. A linear mask, 60-pixels wide in the spatial direction and centred on the star's horizontal position, was applied to the detector frame. Sixty pixels removed the stellar influence while maintaining as much OH data as possible. The remaining OH lines do not appear as straight lines on the array due to the intersection of the array detector with the telescope's diffraction optics. Instead they are parabolic, with a curvature

25   that varies linearly with spectral position. To straighten them for integration, a line's spatial and spectral pixels (x,y') were mapped to a coordinate system where the line appears at the same spectral location, y, along the entire spatial extent, x, using the function $y = y'+(x-p_1)^2 \cdot p_2$. The detector is aligned such that the central position of the parabola, p_1, is constant at column number 465, and the curvature, p_2, is given by $p_2 = 3 \cdot 10^{-5} + 5.3 \cdot 10^{-8} \cdot y'$. The result after processing is shown in Fig. 1(b).

Given this transformation, the OH lines could then be integrated in the spatial dimension, x, for a given value of wavelength,

30   y, with the standard deviation used to estimate each line's uncertainty, to form a high signal-to-noise spectrum (after accounting for the pixels masked out as described above). A Gaussian function with a width of 0.31 nm was found to fit the line shape of the resulting OH lines in the *H*-band spectral region to within the noise present in the data.

Since the wavelengths of the OH lines are known (Rothman et al., 2013), and the lines are easy to identify, the abundant lines themselves were used for wavelength calibration. The brightest lines of the Q-branch and the six brightest P-branch lines of each transition in a spectrum were used for this calibration. For the *H*-band example presented here, this led to a calibration based on 22 pixel/wavelength pairs (only the main Q-branch lines were used for the (6,4) transition). The wavelength calibration has only small nonlinear contributions.

3 Results

3.1 *H*-band data

In Fig. 2 the resulting *H*-band spectrum is shown based on the total integration time of 10.8s. The flat-fielding distorts the edges of the spectrum slightly as the filter transmission nears zero in the red highlighted regions in the figure. At the long-wavelength end, the Q- and R-branches from the (6,4) transition can be seen. The other three resolved bands belong to the (3,1), (4,2) and (5,3) transitions. The signal-to-noise ratio is 280 for the Q-branch lines and around 200 for the P-branch lines for this 10.8 s exposure. Longer integration times increase these ratios further. The pixel intensity in analog-to-digital units (adu) is directly proportional to the photon count rate at these low intensities that are within the linear range of the detector.

As can be seen in Fig. 2, the background is not completely flat but has low frequency variations that span a wavelength range greater than the OH line widths. Since these background variations will influence the relative intensities of the individual rotational lines, they can impact the fitted OH rotational temperature as the temperature is strongly dependent on the relative heights of the lines. For this reason a 7-order Butterworth IIR filter with a cutoff (-3dB point) at $\frac{1}{3.3 nm}$ was applied to the extracted 2D spectra to remove the low frequency variability. This filter was optimised through repeated tests on synthetic OH spectra to have minimal impact on the OH rotational lines. Fig. 3a and b show the (5,3) vibrational band before and after application of this filter. After filtering, the spectrum was normalized such that the absolute area under the spectrum was equal to one.

A model spectrum was created using the known OH line strengths, $S_{j'j''}$ for a given vibrational transition (Rothman et al., 2013), assuming a Boltzmann distribution of the upper-state rotational levels:

$$I = N_{v'} \cdot S_{j'j''} \cdot (v_{j'j''})^3 \cdot \exp\left(-\frac{E_{j'}}{kT_{\mathrm{rot}}}\right)$$

Here $N_{v'}$ is the relative population of the upper vibrational level, v', and $v_{j'j''}$ is the wavenumber of the transition from the upper state level at potential energy $E_{j'}$ to the final rotational state at energy $E_{j''}$. To form the model spectrum, these relative line intensities were convolved with the instrumental line shape, then filtered and normalized in the same manner as the data. A χ^2 minimisation using the rotational temperature and a total intensity scaling factor as the variable parameters was then performed between the model and the data to determine the rotational temperature best fitting the data. A Brent algorithm (Brent, 1973) from the GNU Scientific Library (Galassi and Gough, 2009) was used for the minimisation. Following Pendleton

et al. (1989), only rotational lines originating from levels $N \leq 4$ were used in the fitting, since higher levels may not be thermalized. The temperature fitting routine was tested against model data varying between 150 and 400 K and was found to reproduce accurate rotational temperatures.

Fig. 3(c) shows the data from Fig. 3(b) along with the fitted model spectrum shown as the red line. The fitted temperature in this case is found to be 188.0 ± 0.56K, representing a 0.3% relative uncertainty. The residual spectrum (data - fit) is shown in Fig. 3(d), where it may be seen that although it appears that the instrumental line shape may not be completely Gaussian, the fitted spectrum accurately represents the observation. This demonstrates that the model used is robust, that fitting the high pass filtered data works well, and that the fit to the data converges to a temperature with a small error when spectra are extracted from an observation based on just 10.8s of total integration time.

3.2 Other vibrational bands

Fig. 4 shows an overview of all the measured OH vibrational transitions recorded in the *H*-, *J*- and *K*-band spectra taken toward the same standard star, extracted in the manner outlined above. All spectra were taken with the same 10.8s integration time and are normalised to the same Q branch intensity for comparison. For the majority of vibrational transitions, the signal is very much greater than the noise, providing excellent data for temperature fitting, especially for the transitions in the H and *K* bands. Since the (7,4) and (8,5) transitions in the *J* band have a Δv=3, the lines are not as intense as in the other Δv=2 bands. Therefore, the signal-to-noise of the individual rotational lines is lower and the fitted temperature measurements are less precise. However, it should be emphasised that all the data presented here are the result of single 10.8s integration time measurements, and longer integrations (or co-adding multiple images) would enhance the data quality.

3.3 Temperature profile

The peak concentrations of the neighbouring vibrational levels are, on average, separated in altitude by 0.5 km (von Savigny et al., 2012). Even though the absolute peak altitudes are known to vary with season (Gao et al., 2010), they can be taken as constant on the time scales of a few minutes over which this experiment was executed. With the altitude separation information, and a steady-state model using a neutral atmosphere from the Naval Research Laboratory Mass Spectrometer and Incoherent Scatter Radar Empirical model (NRLMSISE) (Picone et al., 2002), the altitude of the (9,7) transition was fixed and the relative altitude of the other vibrational transitions were assigned. The rotational temperatures derived from each of the individual vibrational bands then determine an atmospheric temperature profile similar to what has been done by Perminov et al. (2007). Fig. 5 shows the distribution in altitude for the data presented here together with the temperature profile deduced from NRLMSISE model for the corresponding location and time. The temperature profile from this model reproduces that of our data for the (3,1), (4,2), (5,3), (6,4) and (9,7) transitions. Data for the (7,4) and (8,5) transitions are not shown since, as discussed above, they are of lower quality and produce large fitting errors. While the (8,6) transition is anomalously high, it was found that the P(2) and P(4) lines are partially absorbed by atmospheric H_2O and CO_2 (Jones et al., 2013; Noll et al., 2012). Fitting a synthetic spectrum in which these line intensities were reduced by the atmospheric transmission yields a temperature

approximately 8% higher than the original synthesized temperature. This accounts for the higher fitted temperature of the observed (8,6) band shown in Fig. 5. Using this same technique, the temperatures for all other vibrational-rotational transitions presented in Fig. 5 were examined and found not to be significantly affected by atmospheric absorption.

Using the measurement technique described above, we see a temperature profile decreasing with v', implying a temperature

5   decrease with altitude that corresponds with the NRLMSISE model during winter. This distribution also agrees with previous measurements (Sivjee and Hamwey, 1987; Lübken et al., 1990; Espy and Hammond, 1995; Phillips, 2004;Wrasse et al., 2004; Oberheide et al., 2006; Perminov et al., 2007; French and Mulligan, 2010; Dyrland et al., 2010). However we should point out that there are measurement who show the opposite effect (Liu et al., 2015; Noll et al., 2015)

4 Outlook

10 Near-IR spectroscopy with NOTCam has been performed over the last 13 years toward point-like sources (stars or marginally extended objects). NOTCam, in both spectroscopic and imaging mode, has been mounted and used on the telescope an average of 15% of the observing time between 2003 and 2016, spread fairly evenly throughout the calendar year. Thus, good seasonal coverage is available as indicated in Fig. 6, which shows the distribution of dates between November 2007 and June 2016 when the NOTCam was used for long-slit spectroscopic observations.

15 The spectroscopic mode has been continuous and stable with no change of optical elements, except for the addition of the two broad-band filters, Z and Y, in 2010. There has been a change of detector, most recently in 2007, but each array is well characterized. All data older than one year (the proprietary period at the NOT) are available in the NOT data archive. Fig. 7 shows histograms of the total number of spectroscopic observations taken in the *J*-, *H*- and *K*-bands for each hour indicating nearly uniform coverage in each wavelength region.

20 With this extensive data set, a variety of atmospheric problems can be addressed. One example is to simply generate climatological temperature profiles of the mesopause region from the long-term data as in Fig. 5. High quality, long-term observations of the mean state, trends and inter-annual variability of this region are rare, especially at low latitudes, and can serve as an important standard against which whole atmosphere models can be validated.

Additionally, there is a long-standing discussion as to whether the vibrationally excited OH quenches to the ground state

25 ("sudden death"), or relaxes to the next-lowest vibrational level (McDade, 1991). Knowledge of the population and quenching of the individual upper states is essential for the interpretation of the OH airglow emission for remote sensing of the mesopause region. These high quality data described above, together with a steady-state model, can be used to estimate the ratio of single to multi-quantum quenching efficiency accurately. Although these quenching rates have been examined by Xu et al. (2012) using broad-band SABER measurements that combine multiple high-v' and low v' levels, the individual bands resolved by

30 astronomical telescopes would allow an unambiguous assessment of these rates.

The data discussed here have very short integration times. This means that a series of measurements of the same spot of the sky can scan the OH layer with a repetition rate of down to 20 seconds. This lies well below the upper boundary of gravity

waves (Kovalam et al., 2011) and stretches into the domain of acoustic and infrasonic waves. Although these waves have been observed in the hydroxyl airglow (Bittner et al., 2010; Pilger et al., 2013), the large spatial resolution of the observations creates ambiguity in their identification. Here the observations have a spatial resolution on the airglow layer of about 100m, sampled with approximately 1000 pixels in the spatial direction of the NOT detector. This high resolution, in both the temporal

5 and spatial dimensions, allows high frequency waves to be measured at a commensurate spatial resolution, and opens up new possibilities to study the smallest structures of waves propagating through the OH layer in the MLT.

Finally, in parallel with the atmospheric work, it will be possible to quantify how the intensity of the mesospheric OH background in the astronomical *H*-, *J*- and *K*-bands varies on different timescales (from minutes to years) over La Palma. This will be useful in the planning and scheduling of observations in order to optimize dithering strategies and observing modes,

10 especially important for instruments observing simultaneously at optical and infrared wavelengths.

Acknowledgements

This work was based on observations made with the Nordic Optical Telescope, operated by the Nordic Optical Telescope Scientific Association at the Observatorio del Roque de los Muchachos, La Palma, Spain of the Instituto de Astrofisica de Canarias. We thank the staff from the NOT for their help and support during a visit by CF in November 2014. This work was

15 supported by the Research Council of Norway/CoE under contract 223252/F50.

References

Abbott, T. M., Aspin, C., Sorensen, A. N., Norregaard, P., Andersen, J., Andersen, M. I., van der Bliek, N. S., Clasen, J. W., Cox, G. C., Klougart, J., Larsen, H. H., Michaelsen, N., Noel, B., Olofsson, G., Perez, C., and Schwarz, H. E.: SWIR at the Nordic Optical Telescope: NOTCam. In: Optical and IR Telescope Instrumentation and Detectors, Iye, M. and Moorwood, A.

20 F. (Eds.), SPIE Proc. Vol. 4008, Munich, 2000.

Baker, D. J. and Stair Jr., A. T.: Rocket measurements of the altitude distributions of the hydroxyl airglow, Phys Scripta, 37, 611-622, 1988.

Bittner, M., Höppner, K., Pilger, C., and Schmidt, C.: Mesopause temperature perturbations caused by infrasonic waves as a potential indicator for the detection of tsunamis and other geo-hazards, Nat Hazards Earth Syst Sci, 10, 1431-1442, 2010.

25 Brent, R. P.: Algorithms for Minimization Without Derivatives, Dover Publications , Mineola, NY, Book, 1973.

Djupvik, A. A.: http://www.not.iac.es/instruments/notcam/, last access: August 10th 2016.

Djupvik, A. A. and Andersen, J.: The Nordic Optical Telescope. In: Highlights of Spanish Astrophysics V, Diego, M. J., Goicoechea, J. L., González-Serrano, I. J., and Gorgas, J. (Eds.), Springer Berlin Heidelberg, 2010.

Dyrland, M. E., Mulligan, F. J., Hall, C. M., Sigernes, F., Tsutsumi, M., and Deehr, C. S.: Response of OH airglow temperatures to neutral air dynamics at 78°N, 16°E during the anomalous 2003–2004 winter, J Geophys Res-Atmos, 115, 1-11, 2010.

Espy, P. J. and Hammond, M. R.: Atmospheric transmission coefficients for hydroxyl rotational lines used in rotational temperature determinations, J Quant Spectrosc Ra, 54, 879-889, 1995.

Espy, P. J. and Stegman, J.: Trends and variability of mesospheric temperature at high-latitudes, Phys Chem Earth, 27, 543-553, 2002.

French, W. J. R. and Mulligan, F. J.: Stability of temperatures from TIMED/SABER v1.07 (2002–2009) and Aura/MLS v2.2 (2004–2009) compared with OH(6-2) temperatures observed at Davis Station, Antarctica, Atmos. Chem. Phys., 10, 11439-11446, 2010.

Galassi, M. and Gough, B.: GNU Scientific Library Reference Manual - Third Edition, Network Theory Ltd, 2009.

Gao, H., Xu, J., and Wu, Q.: Seasonal and QBO variations in the OH nightglow emission observed by TIMED/SABER, J Geophys Res-Space, 115, 1-13, 2010.

Jones, A., Noll, S., Kausch, W., Szyszka, C., and Kimeswenger, S.: An advanced scattered moonlight model for Cerro Paranal, Astron Astrophys, 560, A91 91-11, 2013.

Kovalam, S., Tsuda, T., and Gurubaran, S.: High-frequency gravity waves observed in the low-latitude mesosphere-lower thermosphere (MLT) region and their possible relationship to lower-atmospheric convection, J Geophys Res-Atmos, 116, 2011.

Liu, W., Xu, J., Smith, A. K., and Yuan, W.: Comparison of rotational temperature derived from ground-based OH airglow observations with TIMED/SABER to evaluate the Einstein coefficients, J Geophys Res-Space, 120, 10069-10082, 2015.

Lübken, F. J., von Zahn, U., Manson, A., Meek, C., Hoppe, U. P., Schmidlin, F. J., Stegman, J., Murtagh, D. P., Rüster, R., Schmidt, G., Widdel, H. U., and Espy, P.: Mean state densities, temperatures and winds during the MAC/SINE and MAC/EPSILON campaigns, The Middle Atmosphere Program/Winter in Northern Europe Project, 52, 955-970, 1990.

McDade, I. C.: The altitude dependence of the OH($X2\Pi$) vibrational distribution in the nightglow: Some model expectations, Planetary Space Sci, 39, 1049 - 1057, 1991.

Meinel, I. A. B.: OH Emission Bands in the Spectrum of the Night Sky. II, Astrophys J, 112, 120-130, 1950.

Noll, S., Kausch, W., Barden, M., Jones, A. M., Szyszka, C., Kimeswenger, S., and Vinther, J.: An atmospheric radiation model for Cerro Paranal, Astron Astrophys, 543, A92, 2012.

Noll, S., Kausch, W., Kimeswenger, S., Unterguggenberger, S., and Jones, A. M.: OH populations and temperatures from simultaneous spectroscopic observations of 25 bands, Atmos. Chem. Phys., 15, 3647-3669, 2015.

Oberheide, J., Offermann, D., Russell, J. M., and Mlynczak, M. G.: Intercomparison of kinetic temperature from 15 μm CO_2 limb emissions and OH*(3,1) rotational temperature in nearly coincident air masses: SABER, GRIPS, Geophys Res Lett, 33, 1-5, 2006.

Pendleton, W. R., Espy, P. J., Baker, D. J., Steed, A., Fetrow, M. P., and Henriksen, E. K.: Observation of OH Meinel (7,4) P(N"=13) transitions in the night airglow, J Geophys Res-Space, 94(A1), 505-510, 1989.

Pendleton, W. R., Espy, P. J., and Hammond, M. R.: Evidence for non-local-thermodynamic-equilibrium in the OH nightglow, J Geophys Res, 98(A7), 11567-11579, 1993.

5 Perminov, V. I., Semenov, A. I., and Shefov, N. N.: On rotational temperature of the hydroxyl emission, Geomagn Aeron+, 47, 756-763, 2007.

Phillips, F., Burns, G. B., French, W. J. R., Williams, P. F. B., Klekociuk, A. R., Lowe, R. P. : Determining rotational temperatures from the OH(8-3) band, and a comparison with OH(6-2) rotational temperatures at Davis, Antarctica, Ann Geophys-Atm Hydr, 22, 1549-1561, 2004.

10 Picone, J. M., Hedin, A. E., Drob, D. P., and Aikin, A. C.: NRLMSISE-00 empirical model of the atmosphere: Statistical comparisons and scientific issues, J Geophys Res-Space, 107(A12), 1468, 2002.

Pilger, C., Schmidt, C., Streicher, F., Wüst, S., and Bittner, M.: Airglow observations of orographic, volcanic and meteorological infrasound signatures, J Atmos Sol-Terr Phys, 104, 55-66, 2013.

Rothman, L. S., Gordon, I. E., Babikov, Y., Barbe, A., Chris Benner, D., Bernath, P. F., Birk, M., Bizzocchi, L., Boudon, V.,
15 Brown, L. R., Campargue, A., Chance, K., Cohen, E. A., Coudert, L. H., Devi, V. M., Drouin, B. J., Fayt, A., Flaud, J. M., Gamache, R. R., Harrison, J. J., Hartmann, J. M., Hill, C., Hodges, J. T., Jacquemart, D., Jolly, A., Lamouroux, J., Le Roy, R. J., Li, G., Long, D. A., Lyulin, O. M., Mackie, C. J., Massie, S. T., Mikhailenko, S., Müller, H. S. P., Naumenko, O. V., Nikitin, A. V., Orphal, J., Perevalov, V., Perrin, A., Polovtseva, E. R., Richard, C., Smith, M. A. H., Starikova, E., Sung, K., Tashkun, S., Tennyson, J., Toon, G. C., Tyuterev, V. G., and Wagner, G.: The HITRAN2012 molecular spectroscopic database, J Quant
20 Spectrosc Ra, 130, 4-50, 2013.

Sigernes, F., Shumilov, N., Deehr, C. S., Nielsen, K. P., Svenøe, T., and Havnes, O.: Hydroxyl rotational temperature record from the auroral station in Adventdalen, Svalbard, J Geophys Res-Space, 108, 1342-1351, 2003.

Sivjee, G. G. and Hamwey, R. M.: Temperature and chemistry of the polar mesopause OH, Journal of Geophysical Research: Space Physics, 92, 4663-4672, 1987.

25 Smith, A. K.: Global Dynamics of the MLT, Surv Geophys, 33, 1177-1230, 2012.

Smith, A. K.: Physics and chemistry of the mesopause region J Atmos Sol-Terr Phys 66, 839 - 857, 2004.

Smith, S. M., Baumgardner, J., Mertens, C. J., Russell, J. M., Mlynczak, M. G., and Mendillo, M.: Mesospheric OH temperatures: Simultaneous ground-based and SABER OH measurements over Millstone Hill, Adv Space Res, 45, 239-246, 2010.

30 Telting, J.: http://www.not.iac.es/instruments/notcam/spectroscopy/, last access: August 10th 2016.

Tody, D.: IRAF in the Nineties, Astronomical Data Analysis Software and Systems II, 52, 173, 1993.

von Savigny, C., McDade, I. C., Eichmann, K. U., and Burrows, J. P.: On the dependence of the OH* Meinel emission altitude on vibrational level: SCIAMACHY observations and model simulations, Atmospheric Chemistry and Physics, 12, 8813-8828, 2012.

von Zahn, U., Fricke, K. H., Gerndt, R., and Blix, T.: Mesospheric temperatures and the OH layer height as derived from ground-based lidar and OH* spectrometry, J Atmos Terr Phys, 49, 863-869, 1987.

Wrasse, C. M., Takahashi, H., and Gobbi, D.: Comparison of the OH (8-3) and (6-2) band rotational temperature of the mesospheric airglow emissions, Rev Bras Geofis, 22, 223-231, 2004.

5   Xu, J., Gao, H., Smith, A. K., and Zhu, Y.: Using TIMED/SABER nightglow observations to investigate hydroxyl emission mechanisms in the mesopause region, J Geophys Res-Atmos, 117, 1-22, 2012.

Yee, J.-H., Crowley, G., Roble, R. G., Skinner, W. R., Burrage, M. D., and Hays, P. B.: Global simulations and observations of O(1S), O2(1Sigma) and OH mesospheric nightglow emissions, J Geophys Res-Space, 102(A9), 19949-19968, 1997.
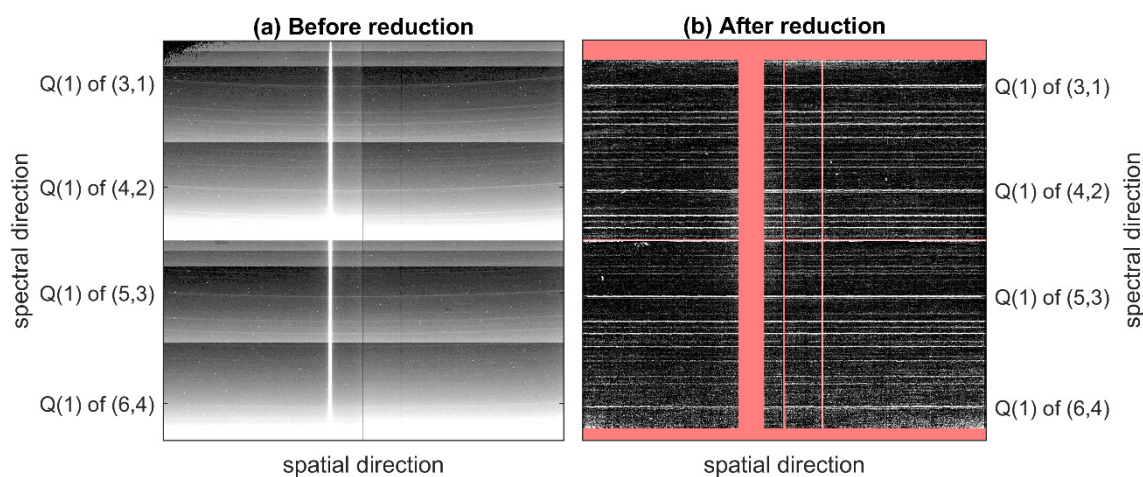
Figure 1: (a) The array in its raw form. The bright star is visible as a vertical band slightly to the left of centre. The curved OH lines are visible in the background. (b) The array after cleaning and flat fielding, with the star removed and the OH lines straightened. The unusable parts of the array are blanked out in red, and the OH lines can be seen clearly.
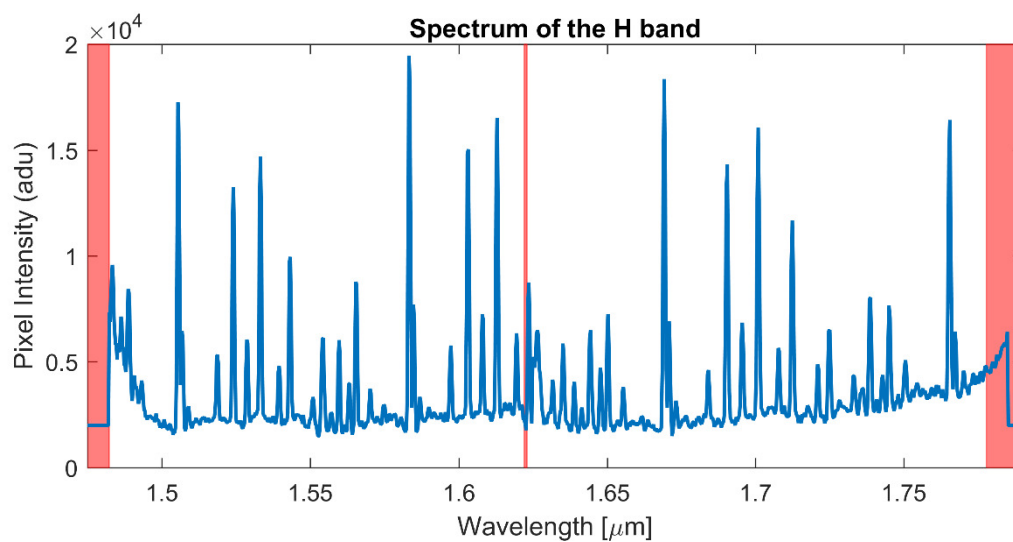
Figure 2: *H*-band spectrum of atmospheric OH extracted from the data frame presented in Fig. 1. Red shading highlights parts of the spectrum not used in the subsequent rotational temperature fitting.
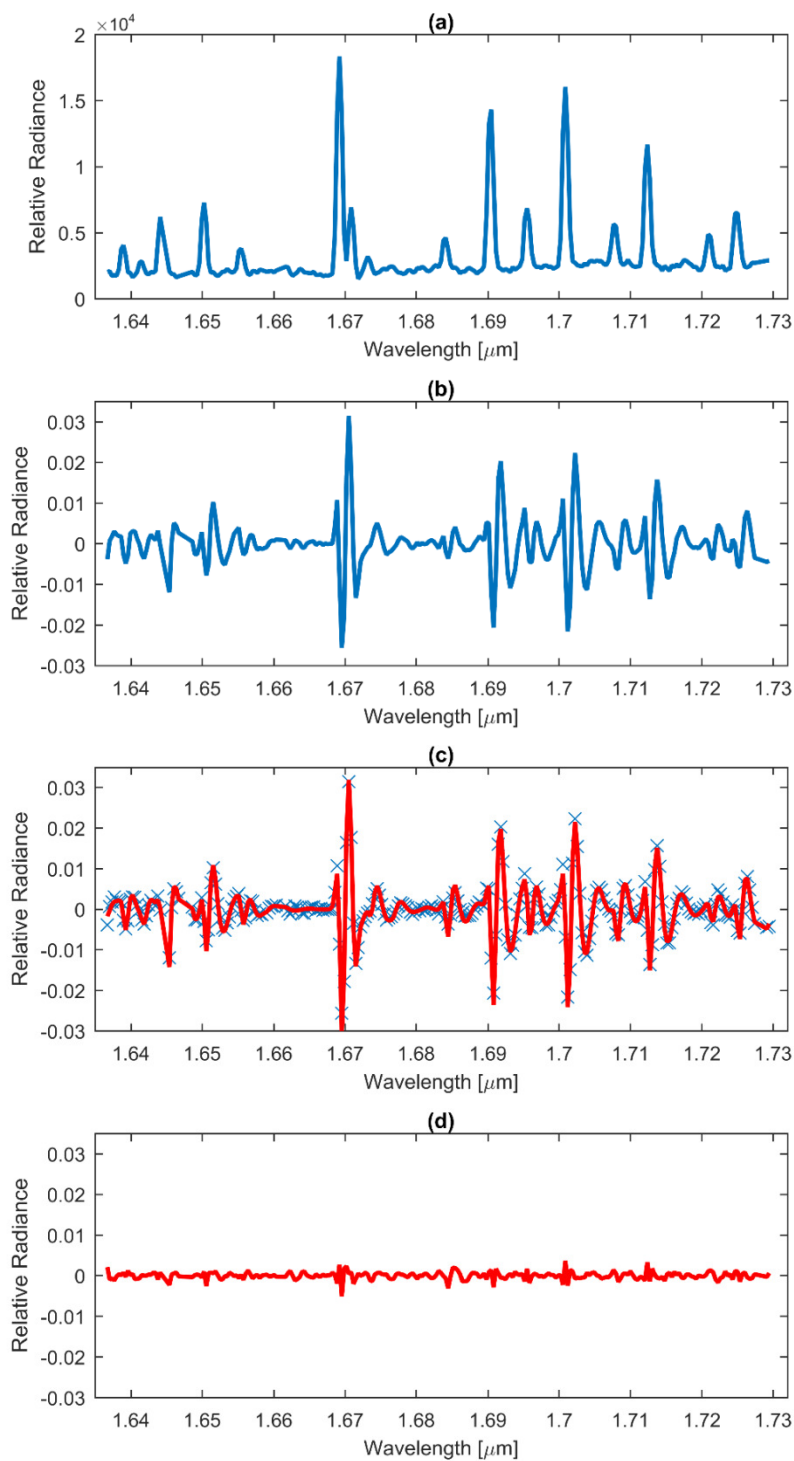
Figure 3: (a) Unfiltered spectrum of the (5,3) transition. (b) Filtered spectrum of the (5,3) transition. (c) Normalised spectrum from Fig. 3(b) (blue crosses) with the fitted, filtered model-spectrum shown in red. The fitted rotational temperature is 188.0 ± 0.56K. (d) Residuals of the fit from Fig. 3(c).
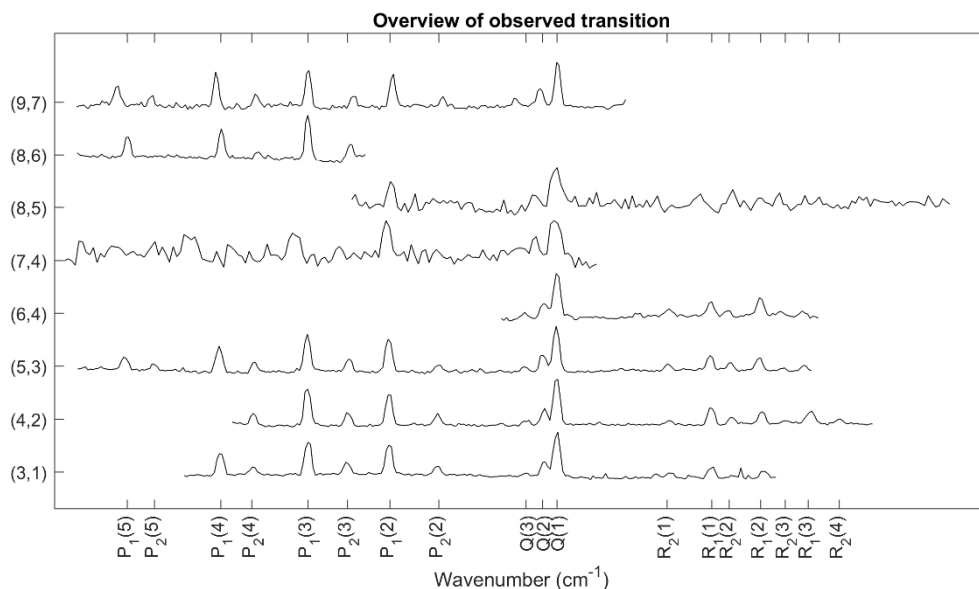
5   **Figure 4: Spectra from the *H*-, *J*- and *K*-bands.**
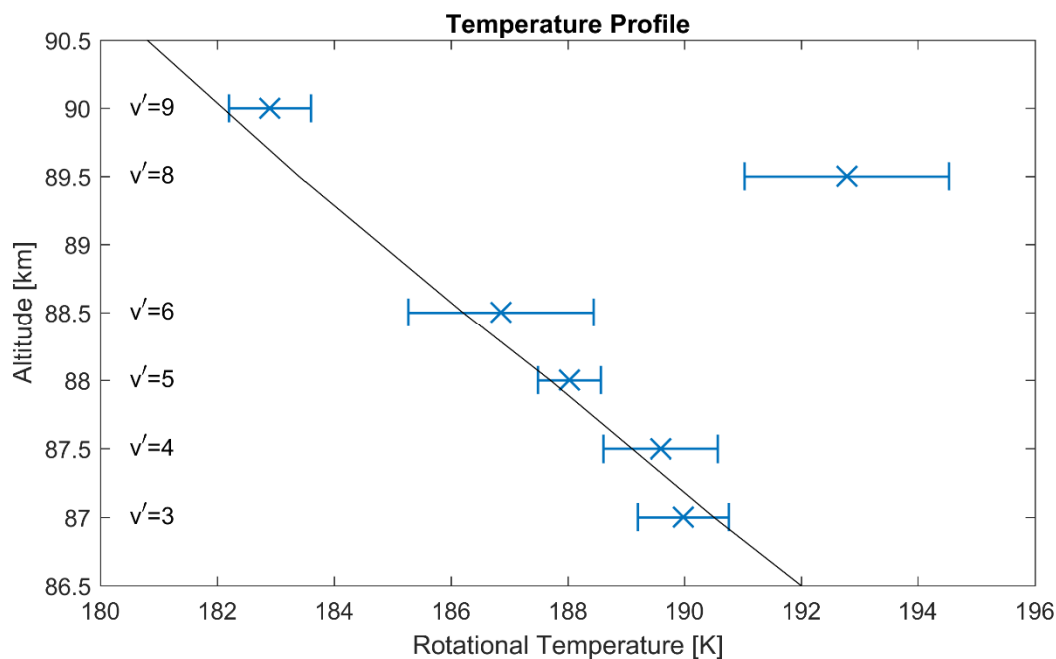
Figure 5: The temperatures from the data presented in Fig. 4 with Δv=2 at their average. The NLRMSISE temperature profile for 2013 February 19 at La Palma (17°53'W, 28°45') at 05:50 UT is shown in black.
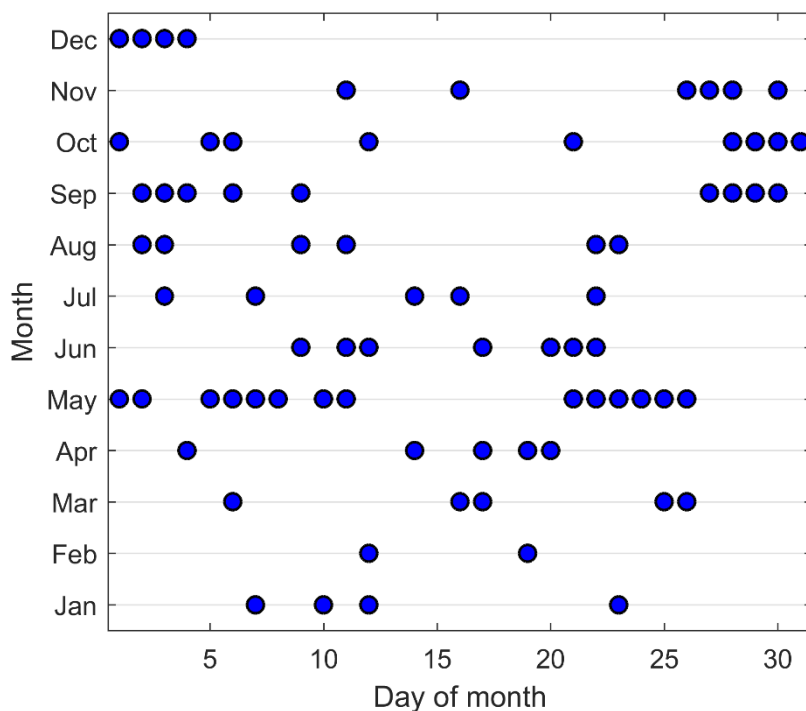
5   **Figure 6: Dates between November 2007 and June 2016 when the NOTCam has been mounted at the NOT and making spectroscopic astronomical observations.**
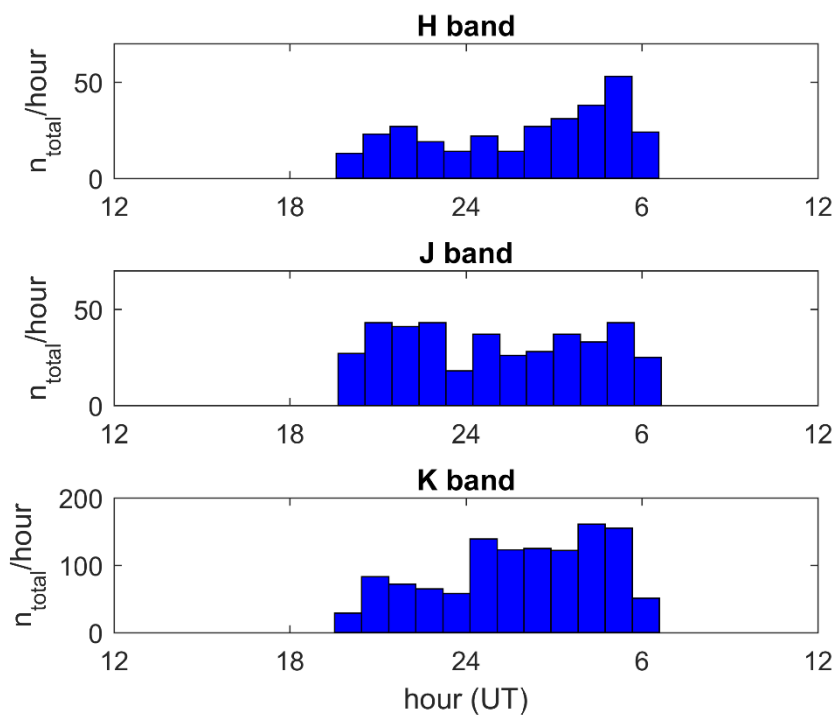
Figure 7: Total number of spectroscopic data frames recorded in each hour and each band with NOTCam between November 2007 and June 2016